An experimental assessment of the effect of current on wave buoy measurements

Coastal Engineering 174 (2022) 104114

Contents lists available at ScienceDirect

Coastal Engineering

journal homepage: www.elsevier.com/locate/coastaleng

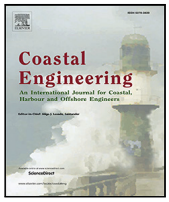

An experimental assessment of the effect of current on wave buoy measurements

S. Draycott [a,*], A.C. Pillai [b], R. Gabl [c], P.K. Stansby [a], T. Davey [c]

[a] Department of Mechanical, Aerospace and Civil Engineering, University of Manchester, Manchester M60 1QD, UK
[b] Renewable Energy Group, College of Engineering, Mathematics and Physical Sciences, University of Exeter, Penryn Campus, Penryn TR10 9FE, UK
[c] School of Engineering, FloWave Ocean Energy Research Facility, Institute for Energy Systems, The University of Edinburgh, Edinburgh EH9 3BF, UK

ARTICLE INFO

Keywords:
Wave measurement buoy
Wave–current interaction
Vortex-induced motions
Experimental testing
Potential flow modelling
Hydrodynamics

ABSTRACT

Wave measurement buoys provide characterisation of wave climates that forms the basis for the design of offshore systems. These buoys are commonly subjected to currents which affect the resulting wave measurements, and if not accounted for will result in errors in the estimated sea state parameters. The present work provides results and observations from experiments aimed at assessing the impact that currents have on wave buoy measurements, thereby informing processing techniques to more accurately include this effect. Through scaled testing (circa 1:15) in a combined wave–current test tank, buoy motions (diameter, $D = 0.24$ m) are recorded in current only, waves only, and combined wave–current including oblique conditions. From these, the wave-induced motions are extracted and compared against three prediction methods based on established transfer function approaches as well as a frequency-domain hydrodynamic coefficient (HC) model based on potential flow. The scaled buoy was observed to have large, complex, irregular oscillatory vortex-induced motions (VIM) exceeding the buoy diameter. Both the magnitude and frequency of these oscillations was found to be significantly altered by the mooring stiffness and configuration whilst the addition of collinear waves was found not to affect the magnitude of VIM. Furthermore, due to the lack of VIM heave response and a large difference between the frequencies of the vortex-induced and wave induced horizontal motions, it was found that the VIM did not significantly alter the interpretation of the wave climate for the tested conditions. The HC model was found to accurately capture the observed modified hydrodynamics for opposing wave–current conditions, where larger horizontal motions than (typically) predicted are observed for all frequencies. This behaviour is concluded to result from increased excitation forces owing to the higher wavenumbers. The experiments highlight the potential effects of VIM on wave measurement performance of wave buoys, along with the complex and mooring-dependent nature of the response. Altered dynamics in the presence of currents are described which must be accounted for to avoid errors and the presented prediction methods provide a mechanism to account for these effects in wave processing methodologies which can subsequently reduce uncertainty in our understanding of the offshore environment.

1. Introduction

Waves and currents interact with each other (Jonsson et al., 1970; Peregrine, 1976; Smith, 1997; Olabarrieta et al., 2010) to produce complex (e.g. Chen and Zou (2019)) and potentially hazardous (e.g. White and Fornberg (1998), Toffoli et al. (2013)) ocean conditions. The resulting combined wave–current conditions effectively determine the hydrodynamic loading experienced by offshore structures and platforms and hence, to design such systems effectively, it is paramount that this combined environment is well understood (Bruserud et al., 2018).

In order to design offshore systems for the appropriate wave–current conditions that they will be subjected to, measurements are required. These measurements may be used directly to inform design, or to validate numerical models able to expand the temporal and spatial scales used for analysis. These models may incorporate the presence of current (e.g. Lewis et al. (2019), Song et al. (2020)), however, typically models only capture waves (e.g. Bunney (2011)). Wave buoys are typically used to validate these wide-area models (Bunney, 2011; Lewis et al., 2019; Song et al., 2020) as they are the most widely used system of measuring ocean waves (Tucker and Pitt, 2001). However,

* Corresponding author.
E-mail address: samuel.draycott@manchester.ac.uk (S. Draycott).

https://doi.org/10.1016/j.coastaleng.2022.104114
Received 5 July 2021; Received in revised form 17 December 2021; Accepted 12 March 2022
Available online 25 March 2022

it is well known that wave buoys are affected by the presence of currents (Gonzales, 1984; Tolman, 1990; Wang et al., 1994; Masson, 1996) and it has been recently shown that even if the buoy perfectly captures the surface elevation, standard post-processing methods will result in significant errors in several key parameters (including wavelengths, steepness, power, directionality) as a result of the unknown current-induced modification to the dispersion relation due to the Doppler effect (Pillai et al., 2021). Recently, wave buoys have been developed which can also simultaneously measure currents (Macisaac and Naeth, 2013; Veras Guimarães et al., 2018). These, in theory, will enable improved sea state parameters to be estimated if the correct approaches are used to process the data. However, even with these measurements modifications to the buoys dynamic response at the wave frequencies will not be considered, resulting from changes to the associated wavenumbers (and fluid accelerations) or from vortex-induced motions (VIM); which are known to affect the motions of floating spheres in current (Govardhan and Williamson, 2005; Sareen et al., 2018b). Additionally, the vast majority of wave buoy datasets used do not have the corresponding current measurement and estimated sea state parameters will be incorrect when there is a current present. To this end, a framework has been developed in Pillai et al. (2021) to estimate current from buoy motions in order to account for it in post-processing. This method also has the ability to include the modified dynamic buoy response if it can be effectively represented by frequency-domain transfer functions.

The aim of the experiments presented herein is therefore to assess the effect of current on wave buoy measurements. Scaled experiments are carried out at the FloWave Ocean Energy Research Facility (FloWave), Edinburgh, UK. This circular basin enables the generation of waves and currents at arbitrary angles to each other (Draycott et al., 2020, 2018a) and hence is well suited to generate a range of conditions to assess the resulting response. Current-only, wave-only, and combined wave–current conditions are presented including oblique cases. Simplistic regular waves are used to isolate the frequency response and simplify analysis.

The aims of the analysis are (i) to assess the effect of VIM on buoy measurement performance, and (ii) to assess the alteration of the buoy dynamics due to current and wave–current interaction. A third aim (iii) is to assess whether the wave-induced buoy motions (x, y, z) can be predicted using simple approaches suitable for incorporating into the aforementioned analysis framework (Pillai et al., 2021). Three methods are assessed. The first method uses the standard linear transfer functions (assuming the buoy behaves as a floating particle) used in buoy post-processing to relate the horizontal motions to the heave motions (see e.g. Benoit et al. (1997)), ignoring the effect of current. This approach will give an indication of the errors typically incorporated. The second approach trialled, modifies the transfer functions to include the correct wavenumbers in the presence of current. For the third approach, a frequency-domain hydrodynamic coefficient (HC) based model is developed, accounting for the effect of current on the buoys mean position (hence mooring stiffness matrix, buoy draught) and on the wavenumbers associated with the observed frequencies in the reference frame of the buoy.

The remainder of the paper is laid out as follows. The relevant theory is described in Section 2, focusing on the modified dispersion relation (Section 2.1) and the hydrodynamic model (Section 2.2). The experimental methodology is outlined in Section 3 including the buoy model and manufacture (Section 3.1), the experimental set-up (Section 3.2) and the test plan (Section 3.3). The main experimental results are presented in Section 4, assessing the response in current-only (Section 4.1) along with wave and combined wave–current conditions (Section 4.2). The methods used to predict the buoy response are compared to experiments in Section 5. Section 6 and Section 7 offer further discussion and concluding remarks respectively.

2. Background & theory

2.1. Wave–current interaction

Current modifies the heights, wavenumbers, and velocities of ocean waves. Of significance for measurements from wave buoys is the change to wavenumbers and velocities, which, unless the current is known, will be incorrectly estimated using the linear dispersion relation considering the wave frequencies observed in the reference frame of the buoy. However, the buoy should still capture the surface elevation, and hence wave heights accurately.

In the presence of a uniform and steady current the wavenumber becomes a function of the current speed and angle relative the current, in addition to the frequency and water depth (Peregrine, 1976):

$$\omega - kU\cos\zeta = \omega_r = \sqrt{gk\tanh kd} \tag{1}$$

where k is the wavenumber, ω is the angular frequency in the fixed reference frame (observed by the moored buoy), d is the water depth and g is the acceleration due to gravity. U is the current speed and ζ is the relative angle between the wave and current fields, where $\zeta = 0$ for waves travelling on a following current. ω_r is the angular frequency observed in a reference frame moving with the steady current.

The group velocity in the fixed reference frame, C_g, can be expressed as:

$$C_g = C_{g,r} + U\cos\zeta = \frac{C_r}{2}\left(1 + \frac{2kd}{\sinh(2kd)}\right) + U\cos\zeta \tag{2}$$

where $C_{g,r}$ is the group velocity in the moving reference frame, and $C_r = \omega_r/k$ is the phase speed in the moving reference frame.

Noting that if U is assumed to be zero there will be errors in sea state steepness $s \propto k$ and power $P \propto C_g$. These are critical parameters for contextualising the hydrodynamic response and performance of offshore systems. In addition, the incorrect assumption of wavenumber will consequently result in errors in the calculated sea state directionality (Pillai et al., 2021).

2.2. Linear hydrodynamic model

A linear hydrodynamic model is developed and compared to both the experiments and linear wave theory (assuming surface tracking) both ignoring and considering the current-modification to wavenumbers. This will enable an assessment to be made of approaches for developing frequency-domain transfer functions which can account for the presence of a current in post-processing.

2.2.1. Hydrostatics

For a wave buoy mounted to the seabed (tank floor) using a single mooring line, the position of the buoy in current can be estimated using a simple force balance in x and z (ignoring rotations). This is depicted in Fig. 1.

To resolve the force balance it is necessary to be able to calculate the submerged volume for the buoyancy force, and submerged frontal area for the drag force, as a function of draught, h. For a partially submerged sphere the submerged volume, V_{sub}, can be expressed as:

$$V_{sub} = \frac{\pi}{6}h(3c^2 + h^2) \tag{3}$$

where $c = \sqrt{h(2R-h)}$ and represents the radius at the waterline, R is the sphere radius and h is the buoy draught.

The submerged frontal area, A, can be calculated using:

$$A = R^2\left(\arcsin\left(\frac{b}{2R}\right) - \frac{b}{2R}\sqrt{1-\left(\frac{b}{2R}\right)^2}\right) \tag{4}$$

where $b = \sqrt{4(2R-h)h} = 2c$.

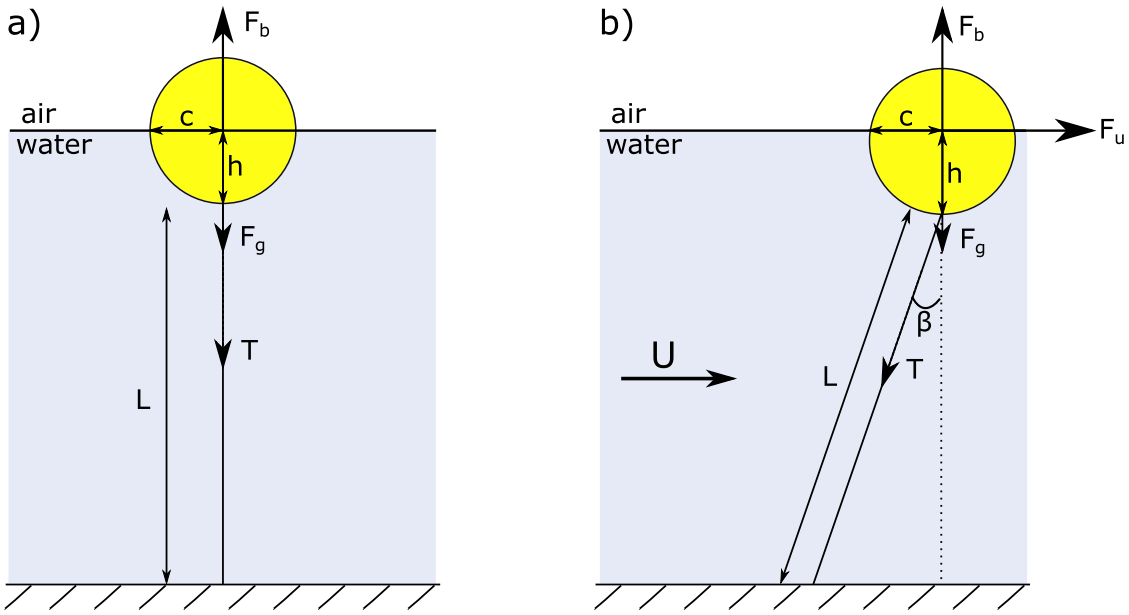

Fig. 1. Diagram showing mean buoy position (a) without, and (b) with, a current present.

In the x direction there is a balance between the drag force from the current, F_u, and the horizontal component of the mooring line tension, T:

$$F_u = \Delta T \sin\beta = k_m \Delta L \sin\beta \tag{5}$$

where ΔT is the difference between the mooring line tension in current and the pretension, and ΔL is the corresponding change to the mooring line length. β is the mooring line angle relative to vertical and k_m is the linear mooring line stiffness. The horizontal force balance can therefore be expressed as:

$$\frac{1}{2} C_D \rho A(h) U^2 = k_m \left(\frac{d-h}{\cos\beta} - L \right) \sin\beta \tag{6}$$

where ρ is the density of water, U is the current velocity and C_D is the drag coefficient. $A(h)$ is calculated using Eq. (4).

In the z direction there is a balance between gravitational, F_g, and buoyancy, F_b, forces along with the vertical component of the mooring line tension:

$$F_b = mg + \Delta T \cos\beta = mg + k_m \Delta L \cos\beta \tag{7}$$

where m is the buoy mass and g is acceleration due to gravity. F_b can be written as $F_b = \rho g V_{sub}$ and as such the vertical force balance can be expressed as:

$$\rho g V_{sub}(h) = mg + k_m \left(\frac{d-h}{\cos\beta} - L \right) \cos\beta \tag{8}$$

where $V_{sub}(h)$ is calculated from Eq. (3).

To calculate the forces acting on the buoy, along with the resulting draught, Eqs. (6) and (8) can be solved simultaneously, with h and β the only unknowns. These are required as inputs to the hydrodynamic model presented in Section 2.2, and are compared directly to experimental measurements in Section 4.1.

2.2.2. Hydrodynamics

The linear hydrodynamic model is a six degree of freedom (6 dof) frequency domain model based on Newton's second law:

$$I\ddot{\epsilon}(t) = F_p(t) + F_r(t) \tag{9}$$

where I is the total inertia matrix (6 × 6) and $\ddot{\epsilon}$ is the acceleration matrix. F_p is the total external pressure force matrix (hydrostatic + hydrodynamic) and F_r is the reaction force matrix including the mooring spring force.

Based on linear theory it is possible to define the acceleration matrix as a function of the frequency-domain displacements, ϵ:

$$\ddot{\epsilon}(t) = \mathrm{Re}\left[-\omega^2 \hat{\epsilon}(\omega) e^{i\omega t}\right] \tag{10}$$

where ω is the angular frequency in the fixed reference frame as in Eq. (1). $\hat{\epsilon}$ are the complex amplitudes of the 6 DoF displacement matrix which comprise of the x, y and z displacements along with the rotations about the x, y and z axes (Θ_x, Θ_y and Θ_z respectively). Θ_x, Θ_y and Θ_z are commonly referred to as roll, pitch and yaw and are depicted on Fig. 2. In subsequent formulations, $\hat{}$ denotes complex amplitude matrices.

In the frequency domain, Eq. (9) can be written as:

$$-\omega^2 I \hat{\epsilon}(\omega) = \hat{F}_p(\omega) + \hat{F}_r(\omega) \tag{11}$$

For our problem the only reaction force is provided by the mooring and hence $\hat{F}_r(\omega) = \hat{F}_m = -K_m \hat{\epsilon}$, where $\hat{F}_m$ is the mooring force and K_m is the mooring stiffness matrix.

The external pressure force can be separated into hydrostatic and hydrodynamic components:

$$\hat{F}_p(\omega) = \hat{F}_{hd}(\omega) + \hat{F}_{hs}(\omega) \tag{12}$$

where $\hat{F}_{hd}$ and $\hat{F}_{hs}$ are the complex hydrodynamic and hydrostatic force matrices respectively. $\hat{F}_{hs} = -G\hat{\epsilon}$ where G is the hydrostatic stiffness matrix. The hydrodynamic force can be separated further into excitation and radiation forces:

$$\hat{F}_{hd}(\omega) = \hat{F}_e(\omega) + \hat{F}_r(\omega) \tag{13}$$

where $\hat{F}_e$ and $\hat{F}_r$ are the complex excitation and radiation force matrices respectively. $\hat{F}_e$ is the excitation force which includes inertia and diffraction effects.

The radiation force can be expressed as:

$$\hat{F}_r(\omega) = i\omega R\hat{\epsilon} + \omega^2 A\hat{\epsilon} \tag{14}$$

where R is the radiation damping matrix and A is the added mass matrix.

To compute the complex displacement amplitudes, the following matrix equation is solved:

$$\hat{\epsilon}(\omega) = \frac{\hat{F}_e(\omega)}{-\omega^2(I + A(\omega)) + G + K_m + i\omega R(\omega)} \tag{15}$$

The open-source boundary element method code Nemoh (Babarit and Delhommeau, 2015) is used to compute $\hat{F}_e$, A, I, G and R for the chosen buoy geometry. In order to obtain meaningful results for the buoy frequency response in the presence of current, the draught, Doppler shifted frequencies and current-modified mooring line angles need to be considered as described below.

2.2.3. Accounting for current: Hydrodynamics

Correcting hydrodynamic coefficients. In Nemoh, hydrodynamic coefficients are calculated as a function of chosen values of angular frequency. The linear dispersion relation (not modified to account for current) is subsequently assumed to compute the wavenumbers which define the velocity potentials used to resolve the hydrodynamic coefficients. As detailed in Eq. (1), the observed frequency in the reference frame of the buoy in current, ω, differs from that in the moving reference frame, ω_r, which is directly related to k through the standard linear dispersion relation.

For Nemoh to use the appropriate wavenumbers associated with a given set of observation frequencies, ω, the associated ω_r values must be provided. To obtain ω_r values associated with the desired set of ω values, first Eq. (1) is solved iteratively to calculate the associated wavenumbers in the presence of current, k. ω_r values can be readily computed by $\omega_r = \sqrt{gk\tanh kd}$. Note that ω is still used in solving the body motions in Eq. (15).

Correcting for draught. To correct for the current-modified draught, Eqs. (6) and (8) are solved to give the buoy draught as a function of the current velocity and mooring set-up (stiffness and initial length). The body is then defined with the appropriate draught before being processed by Nemoh. However, this results in an incorrect calculation of the buoy inertia coefficients as the mass is assumed to be larger than reality to account for the increased draught. To correct this minor discrepancy, the inertia matrix is scaled by the ratio between the actual mass and the mass assumed/calculated by Nemoh.

2.2.4. Accounting for current: mooring

From Section 2.2.1 it is evident that the mooring line angle must change in order to balance the current-induced drag force. Hence, the mooring stiffness matrix needs to be defined to account for this.

To simplify the formulation, the x-axis has been defined parallel to the mean current direction and the effect of rotations have been ignored. Under these assumptions, following Al-Solihat and Nahon (2016), the stiffness matrix, K_m, for a single mooring line can be approximated as:

$$K_m = \begin{bmatrix} k_{11} & 0 & k_{13} & 0 & 0 & 0 \\ 0 & k_{22} & 0 & 0 & 0 & 0 \\ k_{13} & 0 & k_{33} & 0 & 0 & 0 \\ 0 & 0 & 0 & 0 & 0 & 0 \\ 0 & 0 & 0 & 0 & 0 & 0 \\ 0 & 0 & 0 & 0 & 0 & 0 \end{bmatrix} \tag{16}$$

where the matrix components are calculated as a function of the line tensions, lengths, and angles computed in Section 2.2.1:

$$k_{11} = \cos^2\alpha k_m + \frac{T}{L}\sin^2\alpha \tag{17}$$

$$k_{13} = \cos\alpha\sin\alpha\left(k_m - \frac{T}{L}\right) \tag{18}$$

$$k_{33} = \sin^2\alpha k_m + \frac{T}{L}\cos^2\alpha \tag{19}$$

$$k_{22} = T/L \tag{20}$$

for consistency with Al-Solihat and Nahon (2016) $\alpha = \pi/2 - \beta$.

2.3. Buoy motion prediction approaches

As mentioned in Section 1, three theoretical formulations to estimate the $z-x-y$ motions of the buoy were used to assess which approach can predict the buoy motions most accurately in the presence of current. In addition to the buoy motions calculated using the numerical model (Eq. (15)), the theoretical transfer functions typically used are compared to the experimental measurements.

Transfer functions, $H_n(f_w, \theta, U)$, are typically used in directional wave buoy analysis which relate the buoys motions ($n = 1\rightarrow3$) to the underlying surface elevation. Most modern buoys are $z-x-y$ displacement buoys, and hence $n = 1, 2, 3$ corresponds to z, x and y motions respectively.

Wave buoys are often assumed to behave like a water particle in a linear sea state. If it is assumed that the buoy can still perfectly capture the underlying surface, based on linear wave theory, $H_n(f_w, \theta, U)$ for an $z-x-y$ buoy would correspond to:

$$H(f_w, \theta, U) = \left[1, \frac{\cos(\theta)}{\tanh(kd)}, \frac{\sin(\theta)}{\tanh(kd)}\right] \tag{21}$$

noting that in current, the calculated wavenumbers, k, associated with the observed wave frequency, $f_w = \frac{\omega}{2\pi}$, should consider the Doppler shift as per Eq. (1) and hence, for a given wave frequency, are a function of the current speed and relative direction. θ is the wave direction relative to the x-axis. To compare to experimental results, these transfer functions are calculated with and without the consideration of current on the wavenumbers.

To summarise, in Section 5, experimental results are compared to predictions made using:

1. The linear hydrodynamic model (Section 2.2)
2. Linear transfer functions including modification to wavenumbers
3. Linear transfer functions omitting the modification to wavenumbers

noting that (3) above is what will be used by default when processing wave buoy data as the current is typically not known.

3. Experimental set-up and methodology

3.1. Model design and manufacture

The experiments outlined here were all conducted with a spherical wave buoy of diameter, $D = 0.24$ m, under test in the FloWave facility as illustrated in Fig. 2. The experimental dataset was, in part, collected for validation and calibration of numerical modelling activities and the simplified plain spherical form was chosen to provide a generic shape for this purpose. Considering the depth of FloWave, the buoy diameter (approx. 0.5 m to 12 m full-scale), and the conditions tested (Section 3.3) the representative scale is around 1:10 to 1:20.

The model wave buoy was 3D printed in acrylonitrile butadiene styrene (ABS) and waterproofed with an epoxy sealant. The internal space could be accessed through a removable top cover for ballasting purposes, with the centre of gravity 40 mm below the mean water level (Fig. 2). A motion capture "tree" with four reflective markers was affixed to the top cover to provide 6 dof motion data, with origin set to the centre of the spherical body.

The model was deployed with both inextensible and flexible moorings. The inextensible mooring was constructed of 2 mm diameter Dyneema® rope and was assumed to be infinitely stiff for the purposes of this experiment. The length was set to obtain a 30° angle with the vertical when taut (in 2 m water depth). The flexible mooring used 2 mm diameter elastic with a length of 1.7 m when unstretched. The flexible line mooring stiffness (k_m) was measured as 6.73 ± 0.3 N/m.

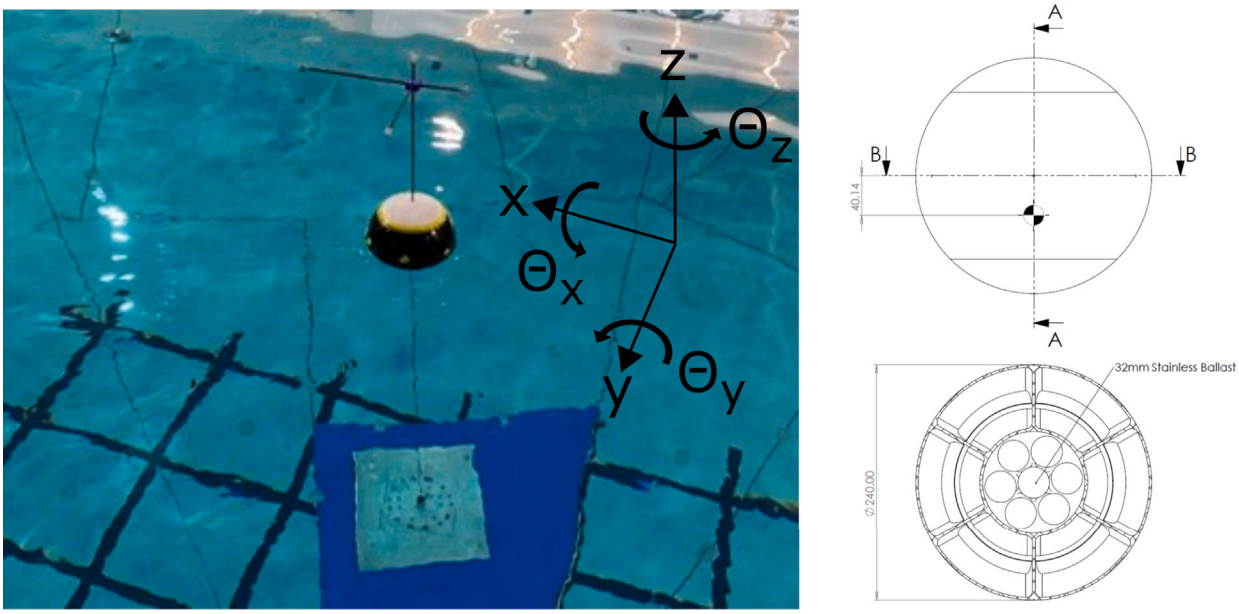

Fig. 2. Buoy and loadcell installed in the FloWave facility. Axes and key buoy dimension indicated.

3.2. Experimental set-up

The experimental programme was undertaken at the FloWave Ocean Energy Research Facility at The University of Edinburgh, UK (circular wave and current tank with a diameter of 25 m and a water depth of 2 m for the upper tank). The model was installed 1.64 m (streamwise) and 0.55 m (cross-tank) from tank centre in order to take advantage of the facility's AMTI OR6-7 floor mounted 6 dof force plate. The force plate was used to measure mooring loads under current, and all instrument locations and motions are referenced from this mooring anchor point, as illustrated in Fig. 3. The 6 dof motion of the buoy was captured based on the Qualisys motion capturing system.

Force plate data (under current only tests) and 6 dof motion data were collected. Additional open tank testing was conducted to characterise the sea states for both wave and current with the wave buoy removed. The tests used twin wire resistance wave gauges and a Nortek Vectrino2 ADV (acoustic doppler velocimeter) measuring at 0.2 m below the still water surface. The locations of these instruments, as per the coordinate system in Fig. 3, are described in Table 1. All instruments were triggered using a 5 V TTL pulse from the wavemakers and hence all systems are synchronised. Wave gauges and motion capture systems were both sampled at $f_s = 128$ Hz, load cell measurements at 256 Hz, and velocity measurements at 100 Hz.

Currents are generated in FloWave using 28 impeller units mounted in a plenum chamber beneath the tank floor (see e.g. Noble et al. (2015)). The turbulence intensity is between 5 and 11% and the vertical shear profile in the centre of the tank follows approximately a 1/15 power law (Sutherland et al., 2017). The turbulence and shear profile strictly violates the aforementioned assumptions of a steady and uniform current, and the shear profile necessitates modification to the dispersion relation and calculation of kinematics (e.g. Jonsson et al. (1978), Kirby and Chen (1989), Li and Ellingsen (2019)) and may affect the mooring dynamics. However, the vertical shear in the tank centre is small, particularly at the low velocities used in these experiments (see Sutherland et al. (2017)) and turbulence for our conditions is small relative to wave-induced velocities. Previous research in FloWave has found the assumption of a steady and uniform current to be effective in the prediction of current-modified wavelengths (Draycott et al., 2018b), kinematics (Draycott et al., 2017), and associated loading on tidal stream turbines (Draycott et al., 2019).

3.3. Test plan

Experiments were carried out primarily to characterise the buoy response in simplified wave, current and combined wave–current conditions. These tests conditions are summarised in Table 2. Tests were initially carried out with different current velocities using both the inextensible and flexible mooring lines to assess the mean positions and response in current (current-only). Current speeds were varied from 0.05 m/s to 0.45 m/s, which corresponds to a Reynolds number $Re = \frac{\bar{U}D}{\nu}$ of between 1.3×10^4 and 1.2×10^5 where $\bar{U}$ is the mean free-stream velocity, D is the buoy diameter and ν the kinematic viscosity of water. Tests of varying wave frequency f_w (0.2 to 0.7 Hz) and a fixed input amplitude a_{in} of 0.03 m were also carried out in the absence of a current (wave-only). Subsequently, combined wave–current tests were carried out for the same f_w and a_{in} values both following and opposing $\bar{U} = 0.2$ m/s current. Lastly, a set of oblique tests were carried out with a fixed f_w of 0.4 Hz and a range of relative angles to a $\bar{U} = 0.2$ m/s current. For all cases with waves only the flexible mooring line was used.

3.4. Test datasets

The test data, including 6 dof wave buoy motions; current induced mooring loads; wave gauge measurements; and ADV velocity data is freely available to download through The University of Edinburgh's Datashare service. The motions and mooring loads can be found at https://doi.org/10.7488/ds/3105 with the empty tank measurements of surface elevation, velocity and bottom pressure at https://doi.org/10.7488/ds/3120.

4. Experimental results

4.1. Buoy response in current only

Tests in current-only conditions were carried out to assess the buoy's mean positions and motions in the absence of waves. The change to the mean positions in the x and z directions are presented in Fig. 4, along with the change in the mean force in the x direction, F_x, as a function of the mean current speed measured by the ADV. Results from both mooring lines are presented along with a comparison to estimates from Section 2.2.1 for the flexible line (with $C_D = 1$ in Eq. (6)). Note

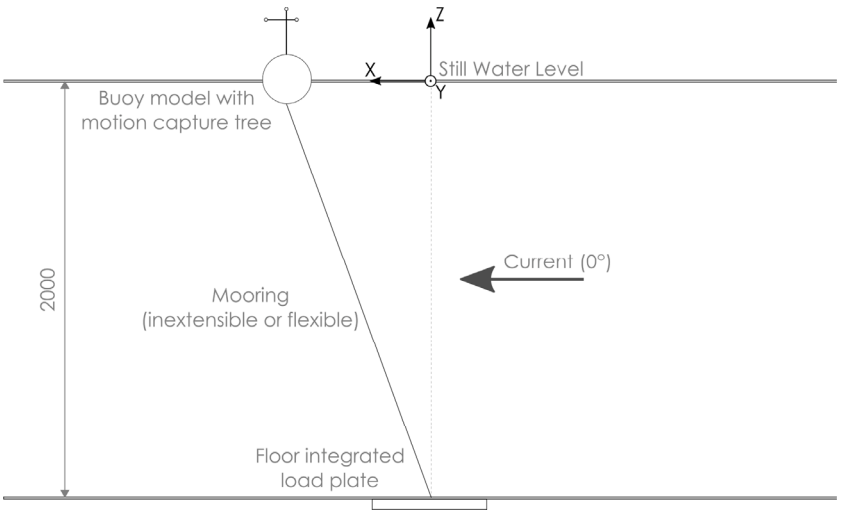

Fig. 3. Test installation schematic with origin and axis system for motion capture measurements and instrumentation locations. All dimensions in mm.

Table 1
Instrumentation locations relative to mooring.

	WG1	WG2	WG3	WG4	WG5	WG6	WG7	WG8	WG9	ADV
x [m]	0.909	0.727	0.273	0.000	−0.091	0.273	0.273	0.273	1.209	0
y [m]	0.000	0.000	0.000	0.000	0.000	−0.273	0.273	1.337	0.000	1.065

Table 2
Wave buoy characterisation test conditions.

Type	Current	Waves	Mooring
Current-only	$\bar{U}$ = [0:0.05:0.45] m/s		inextensible, flexible
Wave-only		a_{in} = 0.03 m, f_w = [0.2:0.05:0.7] Hz, ζ = 0°	flexible
Following	$\bar{U}$ = 0.2 m/s	a_{in} = 0.03 m, f_w = [0.2:0.05:0.7] Hz, ζ = 0°	flexible
Opposing	$\bar{U}$ = 0.2 m/s	a_{in} = 0.03 m, f_w = [0.2:0.05:0.7] Hz, ζ = 180°	flexible
Oblique	$\bar{U}$ = 0.2 m/s	a_{in} = 0.03 m, f_w = 0.4 Hz, ζ = [0:22.5:180]°	flexible

that the current direction was aligned with the positive x axis. As expected for the flexible line, larger mean displacements are observed in the x direction compared to the inextensible line. This is coupled with reduced mean displacement in the z direction due to the smaller vertical component of the line tension required to balance the increased current-induced drag. Conversely, the draught of the buoy attached to the inextensible line increases significantly; increasing the buoyancy to offset the larger vertical component of the line tension. Slightly higher ΔF_x values are measured for the flexible line, which was unexpected due to the increased submergence for the inextensible line, and hence expected increase in the drag force. It is speculated that this discrepancy is a result of velocity variations along the x axis as observed in Noble et al. (2015) coupled with the large changes in mean x position observed (ADV measurements were made at a single location as defined in Table 1). The statics model presented in Section 2.2.1 (solid green line) provides a reasonable agreement with the experimental results, with errors likely arising due to the unaccounted for spatial variation of current velocity.

The standard deviations presented in Fig. 4 demonstrate that there is significant variability around the mean x and z positions. However, the majority of the change in position was observed in the y direction. $x-y$ trajectories of the buoy in different current speeds for both moorings are presented in Fig. 5. Large irregular oscillatory vortex-induced motions (VIM) are observed for both mooring lines. It is evident that larger y motions are observed for the inextensible line than the flexible line, where trajectories at lower current velocities form well-defined arcs determined by the (approximately constant) mooring line length. At larger velocities, the motions with the inextensible line deviate from the arc-like motions and become more chaotic which is expected to be a result of increased (absolute) turbulence inducing additional variations to the buoy draught (z) and $x-y$ positions. For the pre-tensioned flexible line, the trajectories are significantly more chaotic, yet still display the large y motions indicative of VIM.

To quantitatively assess the buoy motions in current-only conditions, standard deviations of the buoy motions in the x, y and z directions as a function of current velocity are presented in Fig. 6. Results for both mooring lines are presented and the mean frequency of oscillation is indicated by the marker shade. From Fig. 6, it is further evident that the y-motions are dominant for both moorings and for some velocities the standard deviations exceed the buoy diameter. Assessing Fig. 6b, peak standard deviations – suggesting resonant behaviour – are observed in the region 0.2 m/s–0.3 m/s for both the inextensible and flexible lines. The y motions are also found to be significantly lower frequency than the x and z motions for both moorings suggesting the VIM is most dominant in the y direction. y-motions for the inextensible mooring are observed to be larger and at much lower frequency (indicated by the marker shade) than the flexible line. Larger z motions are also observed for the inextensible line due to the inability to respond to variations in x-forcing (e.g. turbulence) without a corresponding change to the z position. The results in Figs. 5 and 6 indicate that the total buoy response is due to vortex-induced forcing coupled with the mooring response defined by the stiffness and configuration.

To put the y motions into context with other literature, a second x axis added above Fig. 6b which provides the predicted normalised velocities for the flexible line. Normalised velocity, U^* is defined as:

$$U^* = \frac{U}{f_n D} \tag{22}$$

where f_n is the natural frequency in the y direction. f_n is estimated by $f_n = \sqrt{(k_{22}/m)}$ using the estimate of k_{22} from Eq. (20) after

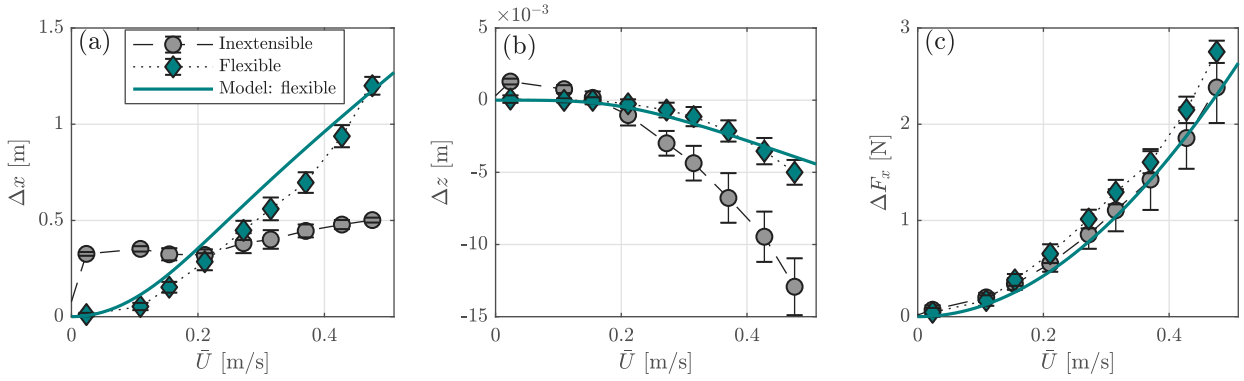

Fig. 4. Mean positions and force in x for the buoy attached to inextensible and flexible mooring lines. (a) mean change in x position as a function of current speed, (b) mean change in z position as a function of current speed, (c) mean change in F_x as a function of current speed. Standard deviations are represented by error-bars. A comparison against the numerical model is presented for the flexible line.

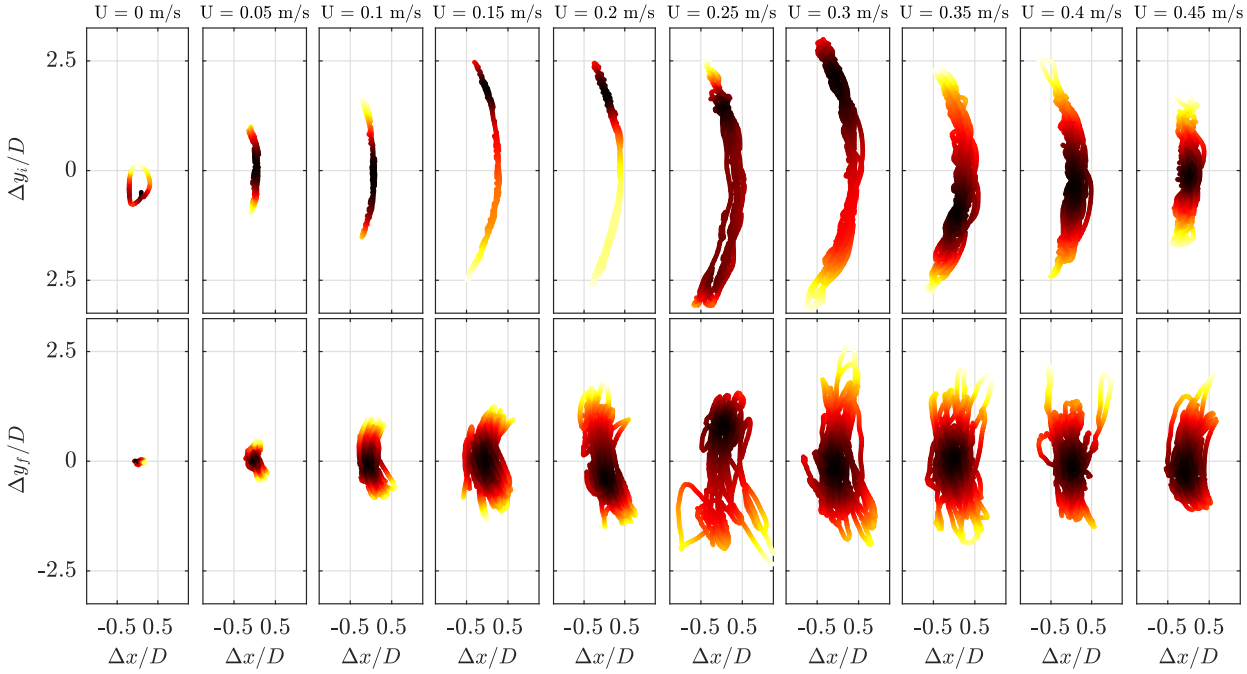

Fig. 5. Buoy trajectories normalised by buoy diameter, D, for both inextensible (top row) and flexible (bottom row) mooring lines. Shown for different current speeds (columns). Colour is proportional to the probability density (black = high probability, yellow = low probability).

solving Eqs. (6) and (8), and hence is a function of U. The values indicate resonant behaviour around $U^* = 10$. Despite the clear effect of mooring line stiffness and configuration on the complex buoy motions, resonance is observed in a similar region to those in Govardhan and Williamson (2005) and Sareen et al. (2018b) for submerged and partially submerged spheres with fixed simplified mountings from above. This suggests that although the mooring alters the buoy response to vortex-induced forcing it does not significantly alter the vortex generation.

Also presented on Fig. 6b (green marker) is the standard deviation of the y-motions calculated over all collinear wave cases (see Table 2) completed at 0.2 m/s; where there is no y-forcing from the waves. The value is calculated over the combined time-series due to the short time-frames of individual wave tests. The error bars denote the standard deviation over the different collinear tests. The y-motion standard deviations appear to be unaffected by the presence of waves, suggesting that (i) collinear wave cases do not appear to break up the vortices significantly, and (ii) there are no additional y-motions introduced from the presence of waves (e.g. due to parametric resonance). The slight differences in the values calculated with and without waves is expected to be a result of differences in test length (300 s for current-only and 22 × 64 s = 1408 s for wave–current cases) coupled with the non-periodic low-frequency VIM (Fig. 6) which require long test lengths to accurately represent statistically. These findings are in agreement with research on the effect of waves on the VIM response of semi-submersible platforms, where the reduction of VIM is found to be negligible for small waves (Martin and Rijken, 2012; Koop et al., 2016) (as in our experiments). It is to be noted, however, that significant reductions in VIM for semi-submersible platforms have been observed in large waves (Hong et al., 2008; Gonçalves et al., 2013) and equivalent results are possible for single-point moored buoys.

4.2. Buoy response in regular waves and regular combined wave–current conditions

4.2.1. Time domain

Example time-series of 6 dof buoy motions in the presence of waves are presented in Figs. 7–10 for wave-only, opposing, following and oblique cases respectively (see Table 2). In Figs. 7–10, the buoy motions

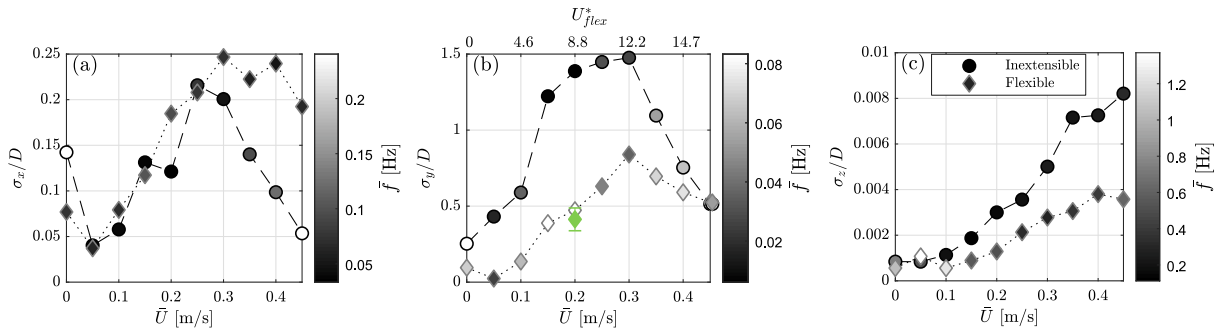

Fig. 6. Standard deviations of motions in x (a), y (b) and z (c) as a function of mean current speed. Shown for both inextensible and flexible moorings. The shade of the markers indicate the mean frequency of the oscillations along the presented axes. The green marker on subfigure (b) is the mean standard deviation of the y motions for all collinear wave cases, whilst the associated error bar represents the standard deviation of the values measured between the collinear cases. A second x axis on subfigure (b) shows the corresponding estimates of normalised velocity U^* for the flexible line.

(black solid line) are shown from 14 s to 38 s for f_w = 0.25, 0.35, 0.45, 0.55 and 0.65 Hz. Also shown (red dashed line) are measurements from wave gauge 3 which is located at the mean position of the buoy in 0.2 m/s current.

Assessing the motions in wave-only conditions in Fig. 7, it is evident that there is good agreement for all frequencies between z motions recorded by the buoy and surface elevations measured using a fixed Eulerian wave gauge. y (sway) motions are found to be negligible and x (surge) motions are found to decrease with frequency as expected due to the corresponding increase in wavenumber. Large x motions are observed for the low frequency 0.25 Hz condition and it appears that there is an additional frequency component (mode of oscillation) in addition to motions at the wave frequency. Assessing the buoy rotations, it is evident that Θ_z (yaw) motions are insignificant, very low-frequency, and uncorrelated to wave forcing. Small high-frequency Θ_x (roll) and Θ_y (pitch) motions are evident for all frequencies, with notable wave-induced Θ_y motions observed for high frequency conditions (0.55 and 0.65 Hz) with corresponding higher steepness' and surface slopes.

Several differences are observed comparing buoy motions in wave-only conditions to those in the same input wave conditions opposing (Fig. 8) and following (Fig. 9) a 0.2 m/s current. For both opposing and following wave conditions, large y motions are observed for all cases and there are low frequency x motions in addition to the wave-induced response. This is consistent with the findings in Section 4.1, and hence are vortex-induced motions still present in the presence of waves. These motions are only semi-periodic and low frequency, and hence vary significantly between the short wave cases. For high-frequency conditions the low-frequency VIM-induced x motions are significantly larger than those induced by waves. These low-frequency displacements are also coupled with Θ_z (yaw) rotations at a visually similar frequency; suggesting that the VIM and mooring interaction causes the buoy to rotate during oscillations. Despite the VIM, good agreement is still found between the buoy z motions and the wave gauge measurements, other than for the high frequency opposing condition presented (0.65 Hz). The reasons behind this are discussed further in Section 5.

The x motion time-series presented in Figs. 8 and 9 are somewhat similar to those induced from nonlinear instabilities for other moored systems (e.g. Gottlieb and Yim (1992), Umar and Datta (2003)) and it is known that some floaters and mooring arrangements subject to waves exhibit complex nonlinear responses, instabilities, bifurcations and chaotic motions (e.g. Gottlieb and Yim (1992), Umar and Datta (2003), Bernitsas and Garza-Rios (1996), Yim et al. (2008)). For our experiments, however, it is evident that the complex x-motions arise from VIM: low frequency motions are uncorrelated to the wave frequency, present for all wave frequencies and relative wave–current angles, and consistent with VIM observed without waves.

Wave–current interaction effects are evident in both Figs. 8 and 9. Wave heights for opposing conditions are found to be larger than the wave-only equivalents as a result of wave–current interaction (e.g. Jonsson et al. (1970)). Similarly, wave heights in following conditions are reduced relative to wave-only conditions. Also evident is the altered group velocities of the waves (increased for following and decreased for opposing): for the 0.55 Hz and 0.65 Hz opposing conditions the stable wave train has not arrived by 14 s, where waves for all frequencies are stable by 14 s for both following and wave-only conditions. Large Θ_y (pitch) motions are also observed for high-frequency opposing conditions due to a combination of the aforementioned increased wave height along with an increase in the wavenumber due to the presence of a current (Eq. (1)) – resulting in larger surface slopes and buoy rotations.

Fig. 10 shows the equivalent time-series for the oblique wave–current conditions. Similar to the collinear conditions, VIM is evident in both the x, y and Θ_z buoy motions. Good agreement is found between wave gauges and buoy z motions, and wave heights are found to increase with relative angle between the wave and current fields due to wave–current interaction. For the non-collinear examples (θ = 45°, 90° and 135°) wave-induced motions are observed in the y direction where VIM is dominant (in addition to the x direction for θ = 45° and 135°). For these conditions the vortex-induced y motions are found to be significantly larger than the wave-induced y motions. Of importance for wave buoy processing and interpretation of the wave field is whether the VIM affects of the amplitudes and phases of the motions at the wave frequencies. This is explored further in Section 4.2.2.

4.2.2. Frequency domain

When analysing buoy data, the z spectrum is used to calculate the frequency spectrum $S(f)$, whilst cross-spectra between the x, y and z motions are used to infer the directional spreading. If there is no z component at a specific frequency (i.e. zero value for $S(f)$) then the x and y motions are inconsequential in terms of the estimated sea state parameters. As the VIM does not introduce a z component, it will only affect the calculation and interpretation of wave parameters if it alters the buoy motions (x, y, z) at the wave frequencies where there are z motions. To assess whether the large VIM motions affect the interpretation of the wave field, Fast Fourier Transforms (FFTs) of the 6 dof buoy signals are presented in Figs. 11–14 for wave-only, opposing, following and oblique cases respectively. To ensure FFTs are representative of the desired wave–current condition, care was taken when calculating FFTs to ensure wave trains were stable and no reflections from the tank walls were present. The start (T_1) and end (T_2) times for FFT analysis for each wave condition were defined as follows:

$$T_1 = T_{ramp} + \frac{R_{tank}}{C_{g,inc}} \tag{23}$$

where T_{ramp} is the ramp-up time, taken to be 4 s, R_{tank} is the tank radius = 12.5 m. $C_{g,inc}$ is the group velocity for the incident wave

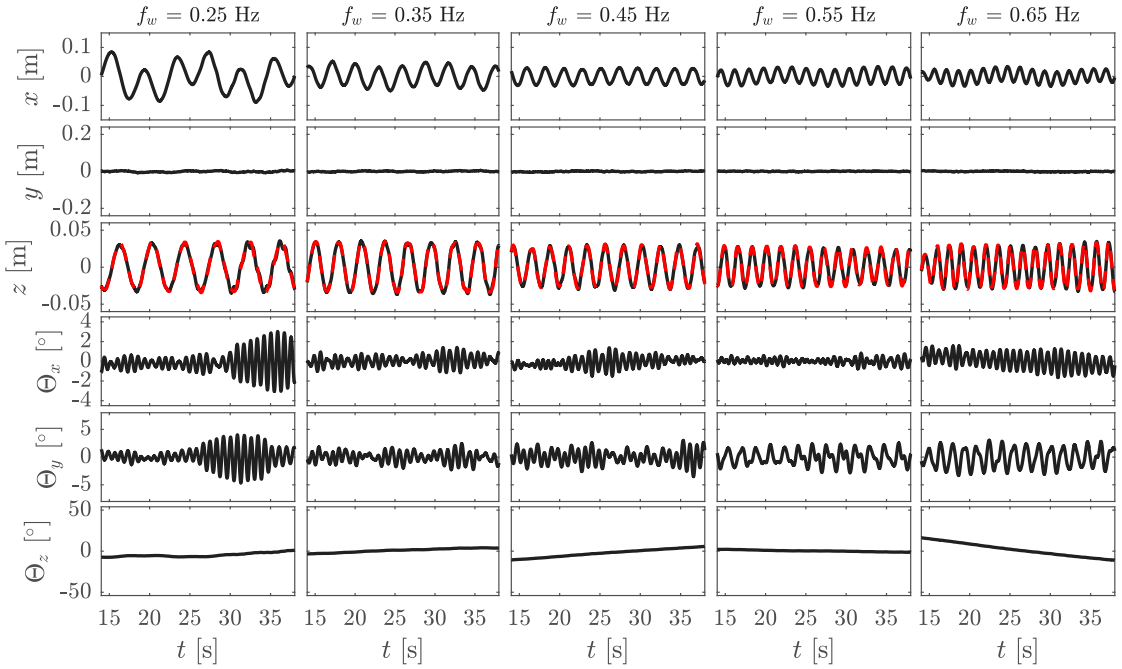

Fig. 7. Buoy displacement and rotation time-series (black solid lines) for different frequencies (columns) for wave-only conditions. Also shown compared to the z motions is the surface elevation measured from wave gauge 3 (red dashed line).

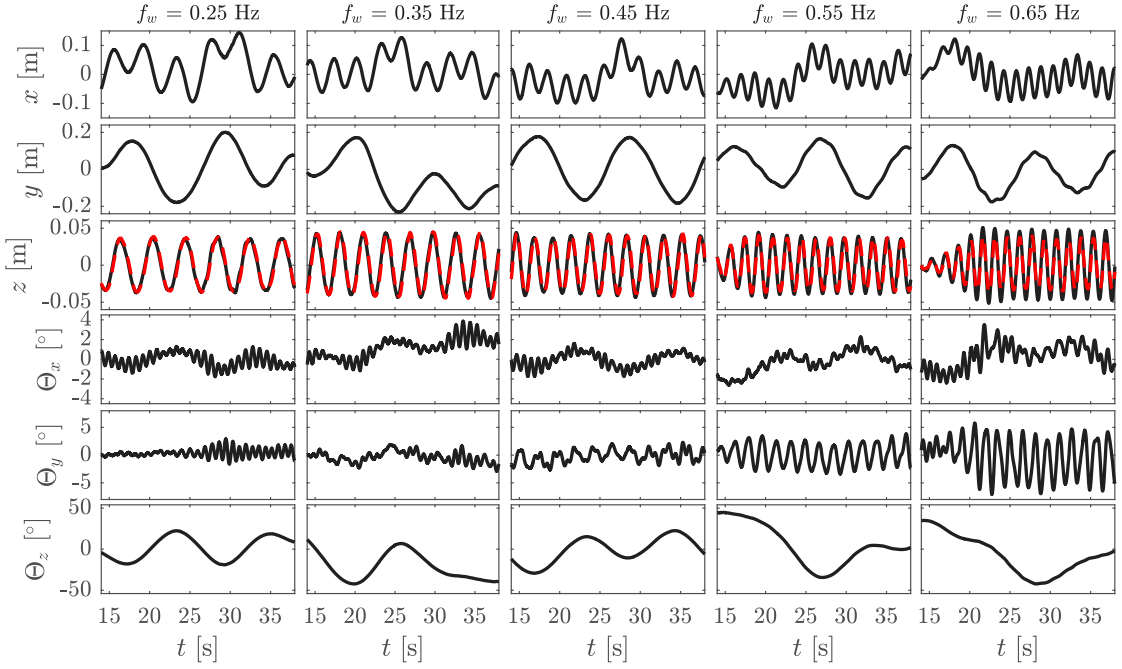

Fig. 8. Buoy displacement and rotation time-series (black solid lines) for different frequencies (columns) for opposing wave conditions in 0.2 m/s current. Also shown compared to the z motions is the surface elevation measured from wave gauge 3 (red dashed line).

calculated using Eq. (2) including the incident k values considering the relative current velocity from Eq. (1). The end time for analysis, T_2, was calculated as:

$$T_2 = T_1 + T_{whole} \tag{24}$$

where T_{whole} is the whole number of regular wave cycles which can be completed before reflections arrive at the measurement location, defined as:

$$T_{whole} = \frac{1}{f}\left\lfloor f\left(\frac{R_{tank}}{C_{g,inc}} + \frac{R_{tank}}{C_{g,ref}}\right)\right\rfloor \tag{25}$$

where f_w is the wave frequency, $\lfloor ... \rfloor$ denotes the floor (round down to nearest integer) and $C_{g,ref}$ is the group velocity of the reflected wave considering the relative current velocity for reflected wave components (assumed to be opposing to incident direction and hence refraction effects are assumed negligible). The nearest measurement time-steps (in 1/128 s increments) to the desired values of T_1 and T_2 were subsequently used for FFT analysis. This approach ensures buoy motions are a result of only incident waves (and VIM) whilst minimising spectral leakage of wave-induced motions in the FFT outputs. This enables extraction of wave-induced motion amplitudes directly from

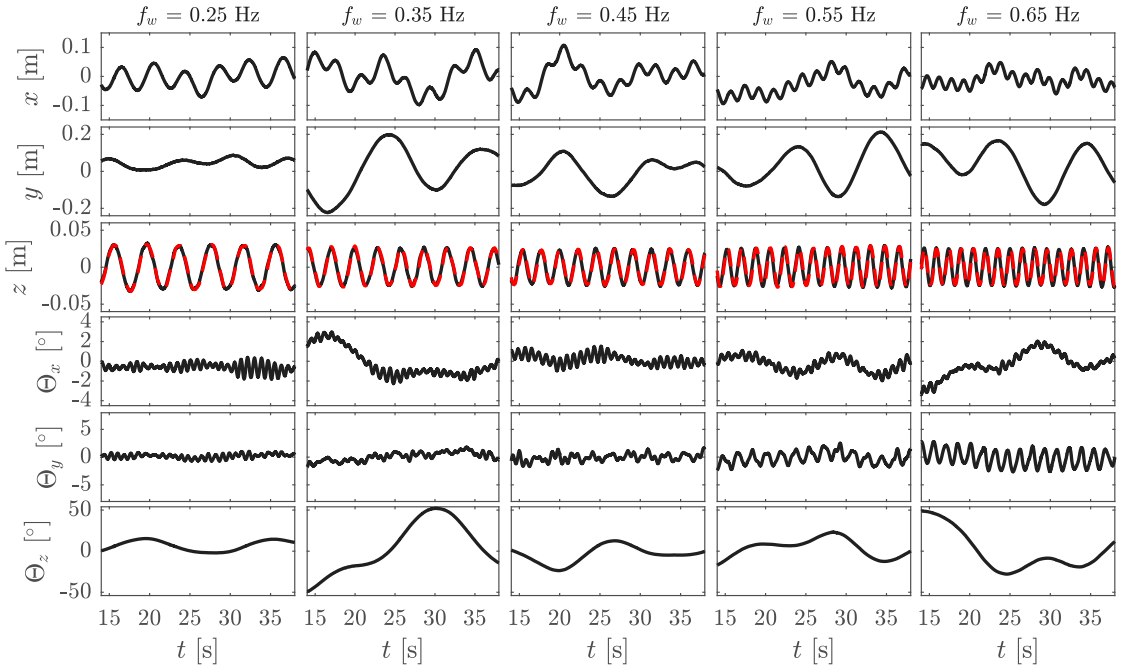

Fig. 9. Buoy displacement and rotation time-series (black solid lines) for different frequencies (columns) for following wave conditions in 0.2 m/s current. Also shown compared to the z motions is the surface elevation measured from wave gauge 3 (red dashed line).

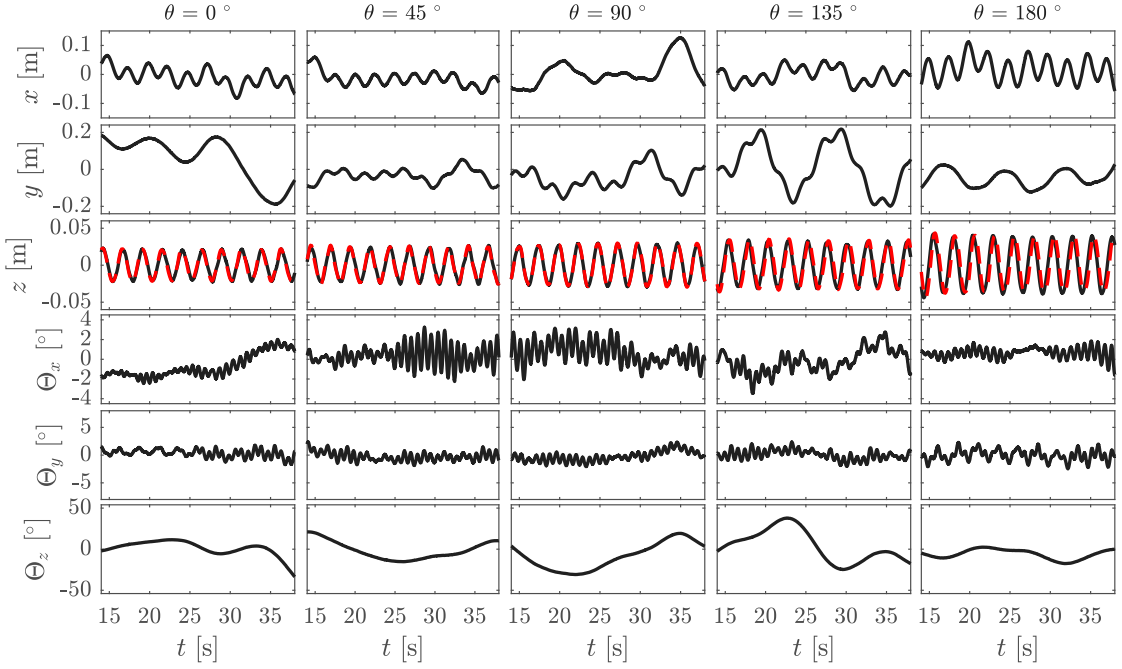

Fig. 10. Buoy displacement and rotation time-series (black solid lines) for relative angles (columns) for oblique wave conditions in 0.2 m/s current. Also shown compared to the z motions is the surface elevation measured from wave gauge 3 (red dashed line).

FFTs for further analysis in Section 5, along with fair comparison to theoretical buoy motion formulations which do not consider the effect of reflections.

Assessing the wave-only FFT outputs in Fig. 11, wave-induced x and z motions are clearly represented in the FFTs along with Θ_y for higher frequency cases with greater steepness. Wave gauge A_z values agree well with those calculated from buoy motions. Wave-induced amplitudes are clearly represented in single frequency bins, yet bins are quite large for low frequency conditions due to the high group velocities and hence corresponding value of $T_1 - T_2$ (frequency bin size $\Delta f = 1/(T_1 - T_2)$). There appears to be a low frequency peak in the A_x spectrum which is likely a mooring response. As expected from Fig. 7, A_y and A_{Θ_z} values are insignificant and high-frequency components are apparent in the A_{Θ_x} spectrum.

Similar to time-domain observations in Figs. 8 and 9 several differences are noted for wave conditions in the presence of a collinear current (Figs. 12 and 13). Large low frequency peaks are observed in the A_x, A_{Θ_z} and particularly A_y spectra corresponding to VIM. The magnitudes and frequencies of the VIM are observed not to be consistent across the conditions due to the short time-frames used for FFT analysis

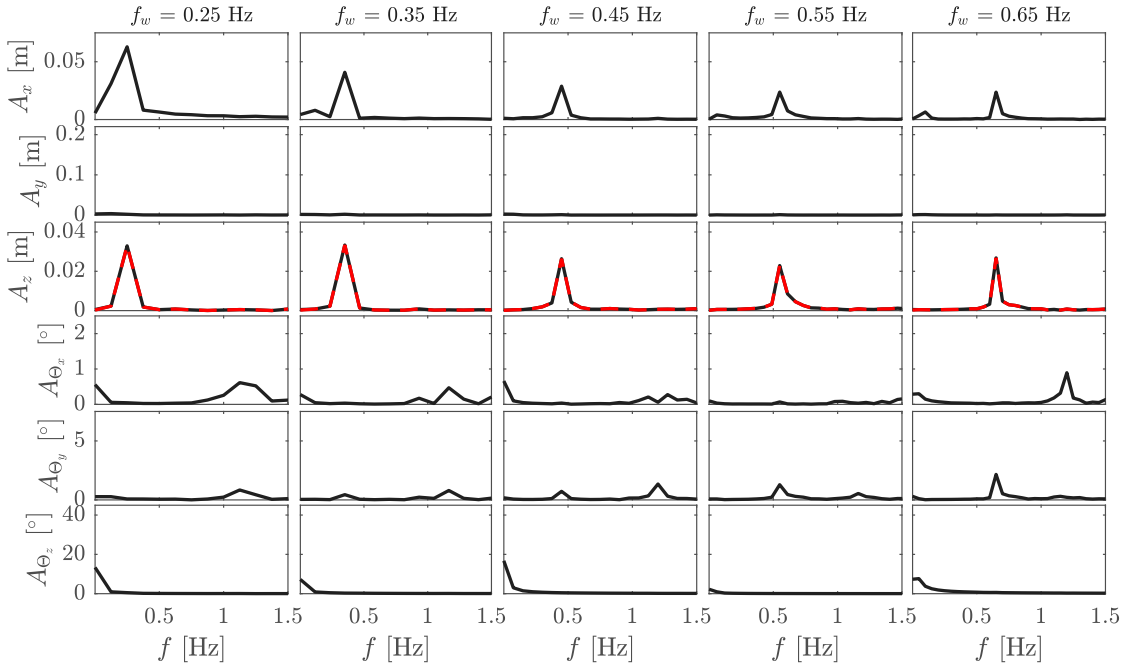

Fig. 11. FFT outputs for buoy displacement and rotations (black solid lines) for different frequencies (columns) for wave-only conditions. Also shown compared to the z motion spectra is the surface elevation measured from wave gauge 3 (red dashed line).

coupled with the low-frequency semi-periodic vortex-induced motions. It is, however, evident that for most conditions (excluding perhaps f_w = 0.25 Hz) there is clear separation in frequency between the wave-induced and vortex-induced x motions. This suggests the VIM will not affect the interpretation of the wave conditions — explored further in Section 5. As expected from Figs. 8 and 9, A_{Θ_y} motions are larger than the wave-only equivalents for opposing conditions (Fig. 12) due to increased steepness, and are correspondingly reduced for following conditions (Fig. 13).

Similar observations are made from the motion FFT outputs for the oblique cases presented in Fig. 14. For the non-collinear examples (θ = 45°, 90° and 135°) where wave-induced y motions are observed in addition to the large vortex-induced y motions, it is evident that the wave-induced components are an order of magnitude smaller than the VIM. Whether this affects the interpretation of the wave climate is explored further in Section 5 and Section 6.

5. Extracted wave-induced motion amplitudes and comparison to buoy motion formulations

The FFT-approach detailed in Section 4.2.2 allows for extraction of wave-induced motion amplitudes which would be challenging to extract from time-series measurements due to the low frequency VIM. Amplitudes were extracted from A_x, A_y and A_z amplitude spectra for all wave and wave–current conditions and are presented in Fig. 15. In Fig. 15 the total wave-induced horizontal response, A_{xy_w}, is presented which is defined as:

$$A_{xy_w} = \sqrt{A_{x_w}^2 + A_{y_w}^2} \tag{26}$$

where A_{x_w} and A_{y_w} are the FFT-isolated motion amplitudes at the wave frequency in the x and y directions respectively. Similarly, A_{z_w} corresponds to the vertical wave-induced motion amplitudes (heave response). Also presented in Fig. 15 are the vertical and horizontal motion amplitudes predicted using the three approaches outlined in Section 2.3. These predictions take amplitudes extracted from FFTs of wave gauge 3 measurements as the underlying surface elevation amplitudes.

Assessing the z (heave) motions in Fig. 15 (top row), it is evident that all prediction methods agree well with each other, and with experiments, other than for high-frequency opposing conditions (as also observed in Figs. 8 and 12). Both transfer function (TF) prediction methods assume that the buoy heave is equivalent to the measured surface elevation (from wave gauge measurements) and hence are identical to each other. Interestingly, the HC model predicts that the heave response in high-frequency opposing conditions will be smaller than the underlying surface elevation; whereas buoy z motions for these conditions are found to exceed surface elevation measurements. This is not expected to be a VIM-effect due to the aforementioned large difference in frequencies. As this is not observed at the same observation frequency for the following and wave-only conditions, it is concluded to be a dynamic response at the wavenumbers associated with these observation frequencies in the presence of opposing current. This may be a result of the higher wavenumbers and steepness for these conditions which could result in non-linear hydrodynamic forcing and response of the buoy: in wave-only 0.7 Hz conditions, steepness, ka = 0.0484 whilst for opposing and following conditions ka = 0.0639 and 0.0364 respectively. These non-linear effects are not accounted for in the linear frequency-domain HC model.

The horizontal buoy motions show increased deviation between the prediction methods and the buoy measurements. For the wave-only conditions, the only deviation between the experiments and prediction methods occurs for low frequency conditions where larger surge motions are measured than predicted. This is concluded to be a resonant mooring response. The HC model predicts these larger motions at these frequencies (if not the precise amplitudes), which are not predicted when mooring stiffness effects are removed from the model. Horizontal motions larger than those predicted using TF methods are also observed for low-frequency conditions in opposing and following currents. Due to the potential for spectral leakage of vortex-induced motions for these low wave frequencies (Figs. 12 and 13) it is not clear the relative contribution of VIM and mooring resonance.

For the opposing-current conditions, larger horizontal motions than TF-approach predictions are observed across all frequencies — where VIM spectral leakage is not present. This is a surprising result and suggests that for opposing conditions (higher k values), the dynamic

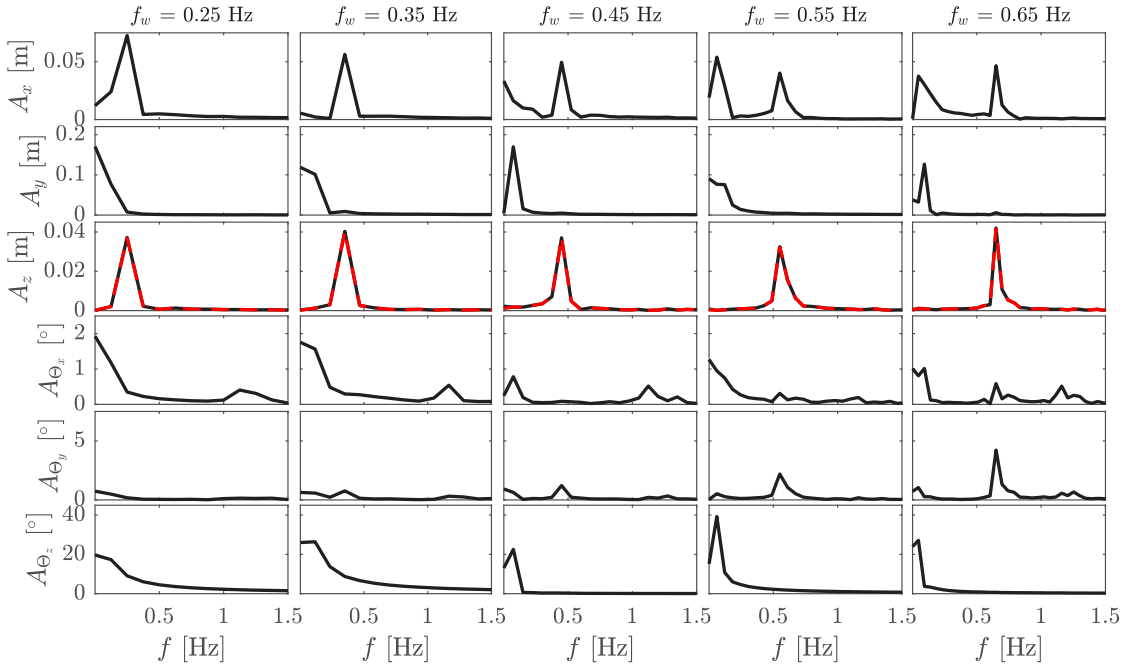

Fig. 12. FFT outputs for buoy displacement and rotations (black solid lines) for different frequencies (columns) for opposing wave conditions in 0.2 m/s current. Also shown compared to the z motion spectra is the surface elevation measured from wave gauge 3 (red dashed line).

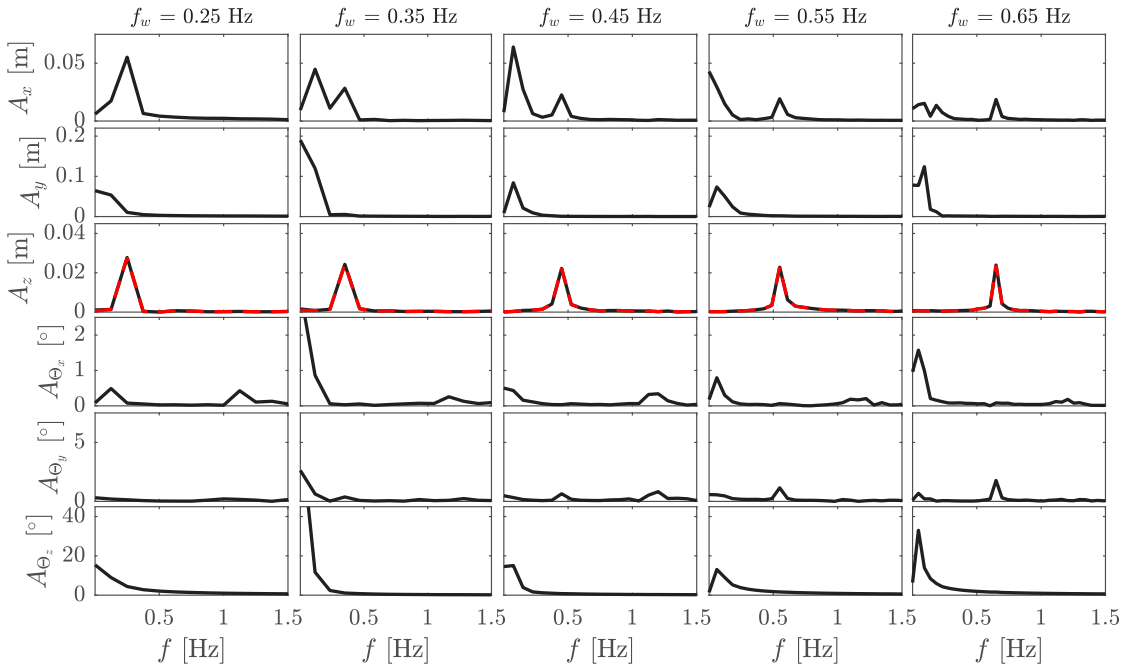

Fig. 13. FFT outputs for buoy displacement and rotations (black solid lines) for different frequencies (columns) for following wave conditions in 0.2 m/s current. Also shown compared to the z motion spectra is the surface elevation measured from wave gauge 3 (red dashed line).

response is significantly altered. Due to the higher wavenumbers for opposing conditions, the horizontal motions were expected to be smaller than those predicted using transfer functions ignoring current ("TF: ignoring current"), however, the opposite was observed. This may be a result of the higher particle accelerations associated with these conditions increasing the excitation force acting on the buoy (see Section 6.2 and Fig. 16 for further analysis). These larger horizontal motions are reasonably well captured by the HC model. Similarly, the opposing and near-opposing cases for the oblique conditions (Fig. 15 left column) show a similarly large horizontal motions which is captured by the HC model.

Assessing the horizontal motions in following conditions, the aforementioned larger low-frequency amplitudes are observed relative to TF-based predictions. In addition, this is coupled with slightly smaller horizontal motions at high-frequencies, which appears to be predicted well with the HC approach.

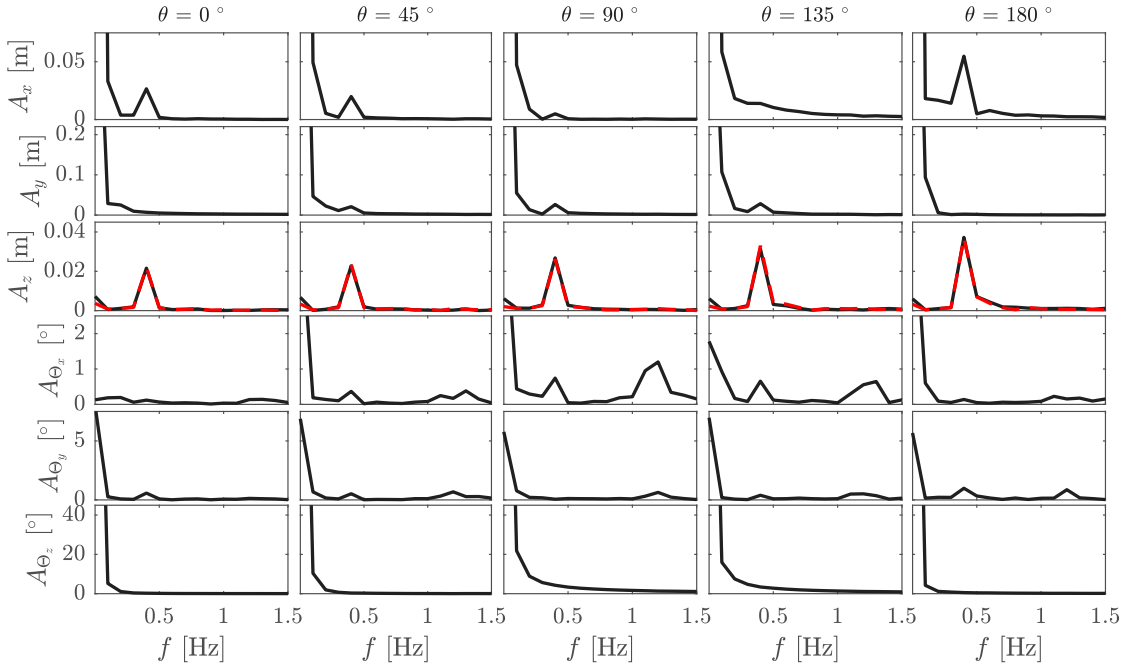

Fig. 14. FFT outputs for buoy displacement and rotations (black solid lines) for different relative angles (columns) for oblique wave conditions in 0.2 m/s current. Also shown compared to the z motion spectra is the surface elevation measured from wave gauge 3 (red dashed line).

In general, it is noted that including current in the transfer-function approaches does not significantly alter the horizontal motion predictions. This is largely a result of the relatively low current velocities which result in modest changes in the predicted values of k with and without the inclusion of current. Additionally, the prediction motions ($\propto 1/\tanh(kd)$) are even less sensitive to changes in current velocity (k). For low frequency conditions, the large wave group velocities results in small changes to the group speed and k values in the presence of current (and hence $1/\tanh(kd)$ values). For higher-frequency conditions in relatively deep water, the sensitivity to k, and therefore current, on prediction horizontal motions diminishes completely as $\tanh(kd) \rightarrow 1$.

6. Discussion

6.1. Vortex-induced motions

For the small wave amplitudes tested, the vortex-induced motions were found to be significantly larger than the wave-induced motions. For most wave conditions tested, however, as there was no vortex-induced heave response and the VIM does not affect the motions at the wave frequencies, it does not affect the interpretation of the wave climate. The exception to this is perhaps the lowest frequency wave conditions (0.2 and 0.25 Hz) where owing to the large frequency bins there appears to some spectral leakage between the frequencies associated with VIM and those associated with wave-induced response. Longer test lengths used for FFTs would mitigate this affect for the experiments presented (as there is a separation in frequencies but is not apparent due to large bins), yet it demonstrates that there are conditions where VIM will affect our interpretation of the waves.

Of relevance for practical wave measurement is the relative importance of VIM for full-scale wave buoys. In the experiments presented, the motions in current-only conditions were found to be complex and non-periodic, and the total motions were found to depend on the vortex-induced forces along with the mooring restoring forces. Both the frequency and amplitude of motions were found to be significantly affected by the mooring system (Fig. 6). These motions are much more complex than those observed for submerged and semi-submerged spheres with fixed mountings (Govardhan and Williamson, 2005; Sareen et al., 2018b), yet despite this, resonant behaviour was found to occur at similar normalised velocities than those previously reported. For full-scale wave buoys the normalised velocity, mooring line configuration, and wave frequencies (relative to frequency of motion in the absence of waves) will largely determine the significance of VIM on the interpretation of the wave climate. The key unknown is the effect of the mooring on the dominant frequencies of motion and hence further work is required; considering buoy-specific geometries and deployment-specific mooring configurations subject to full-scale current and wave conditions including VIM.

An additional challenge in drawing full-scale conclusions on VIM from the presented experiments is that of Re scaling (assuming Froude similitude). The Re values in the presented experiments were $10^4 \rightarrow 10^5$ and are likely to be in the order of 10^7 for full-scale buoys subject to full-scale currents. However, it is expected that this aspect will introduce less uncertainty than the effect of the mooring response on the frequency of motion. This is in part due to the already high Re used in the experiments which significantly exceed many other studies assessing VIM of spheres e.g. Govardhan and Williamson (2005), Sareen et al. (2018b), Behara and Sotiropoulos (2016), Sareen et al. (2018a), Rajamuni et al. (2020), Lee et al. (2008)), where values range from 10^1 to a maximum of 10^4. Additionally, resonance was observed for comparable values of normalised velocity to Govardhan and Williamson (2005), Sareen et al. (2018b) suggesting a negligible dependence on Re, and, in Govardhan and Williamson (2005) Re independence of the results is noted over a Re range from 2000→12000. It may therefore be reasonable to assume negligible influence of Re between model-scale and full-scale behaviour although this remains uncertain due to lack of data of VIM for spheres at high Re numbers. For circular cylinders, however, the magnitude of VIM is known to vary between high sub-critical and post-critical Re (Raghavan and Bernitsas, 2011) which may occur for spheres. Nevertheless, our results indicate that the frequency of VIM is of most relevance for our interpretation of the wave climate, which will be relatively unaffected by Re, but, as shown in this paper, significantly altered by the mooring.

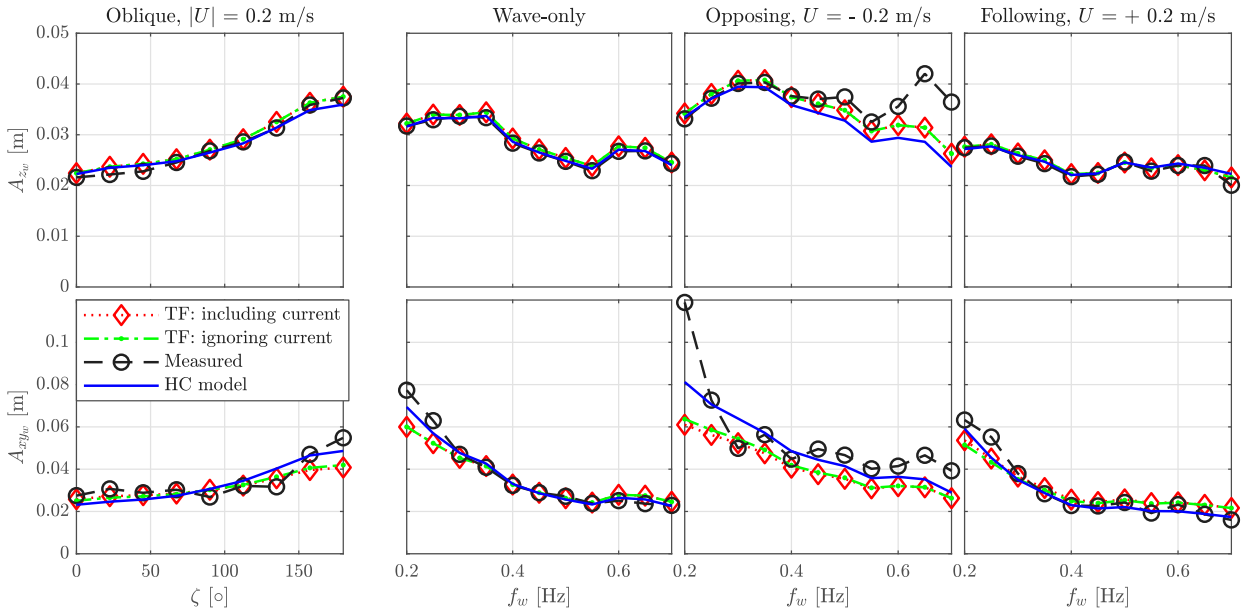

Fig. 15. Vertical (top row) and horizontal (bottom row) motion amplitudes for oblique (left), wave-only (centre-left), opposing (centre-right) and following (right) conditions. Values extracted from FFTs applied to measurements are compared to transfer function approaches and the HC model.

6.2. *Transfer functions for inclusion in wave buoy processing methodologies*

As discussed in Section 1, one of the aims of the paper was to assess which of the three methods outlined in Section 2.3 can be used to predict the horizontal buoy motions in the presence of a known current. If successful, the method(s) can be implemented in buoy processing methodologies (e.g. Pillai et al. (2021)) to estimate the current from the buoy motions alone — from the relationship between the current and the current-modified horizontal motions at each of the wave frequencies.

In Section 5 it was noted that the transfer function approach trialled has low sensitivity to current for the conditions tested, and hence may be unsuitable for estimating low currents from the motions. In shallow and intermediate water there is some sensitivity to current velocity on the horizontal buoy motions which may be sufficient for a reasonable estimation, however, at high-frequencies in deep water the sensitivity diminishes. There is therefore an inherent limit on the applicability of such approaches for inclusion in processing methodologies aimed at resolving the current velocity: to provide an estimate at all, at least some of the wave components must be in intermediate water depth. This is further complicated by the fact that the non-dimensional depth (kd) is not known *a priori* without knowledge of the current itself.

The frequency-domain HC approach tested provided improved estimates for the horizontal buoy motions in the presence of current and hence may provide better estimates of current velocity if the model outputs are utilised as transfer functions. Fig. 16 presents HC-model outputs of horizontal excitation force, added mass, radiation damping and the resulting horizontal motion amplitudes as a function of current speed, frequency and relative angle. Results are presented normalised by the values in the absence of current. It is evident that the hydrodynamic coefficients and the resulting buoy motions have sensitivity to the current even for high frequencies in deep water and hence have wider applicability than linear transfer-function approaches. Assessing Fig. 16, it appears that the large measured horizontal motions in opposing currents (observed in Fig. 15) result from the larger particle accelerations and excitation forces due to the higher wavenumbers, which is captured by the HC model. These factors are not considered in standard transfer-function based approaches.

Owing to the improved motion estimates and larger applicability range, the HC model values appears to be a more favourable candidate for inclusion in buoy processing methodologies. The downsides of using the HC approach is that a large number of transfer functions need to be generated for a specific buoy geometry and mooring configuration. Further work aims to assess the performance, and trade-offs, of both approaches integrated into the methodology presented in Pillai et al. (2021).

7. Conclusions

In this paper, we present the results and observations of an experimental study at the Flowave Ocean Energy Research Facility on the effect of currents on wave buoy measurements. Using a model scale wave measurement buoy (diameter, D = 0.24 m) tested under current-only, wave-only, and combined wave–current conditions, six degree-of-freedom wave buoy motions along with mooring line tensions, surface elevations, and velocity measurements are recorded. From this dataset, the effect of current on the measurement of waves is assessed experimentally and three numerical approaches for predicting the buoy motions in the presence of current are compared to the measurements.

Large, low-frequency vortex-induced motions (VIM) exceeding the buoy diameter were observed for both current only and combined wave–current conditions. The VIM are found to be dominant in the y (transverse) direction, where peak resonant motions are found in the region 0.2–0.3 m/s. This corresponds with a normalised velocity range of 9–12, which agrees well with previous work (Sareen et al., 2018b) with simplified rigid mountings from above. The nature of the buoy motions in current are found to be complex and non-periodic, and the amplitude and mean frequency of VIM is found to be significantly altered by the mooring stiffness and configuration. For the flexible pretensioned mooring, amplitudes are found to be smaller and frequency is found to larger, than those with a inextensible mooring. The addition of collinear waves is found not to influence the magnitude of vortex-induced y motions.

Through spectral analysis it was concluded that, owing to the frequency separation and lack of vortex-induced heave response, the VIM can only affect the interpretation of the wave climate for the lowest frequency wave cases. For the vast majority of experiments the VIM does not influence the apparent wave-induced response, and, consequently, the assumed wave field. However, due to the complexity

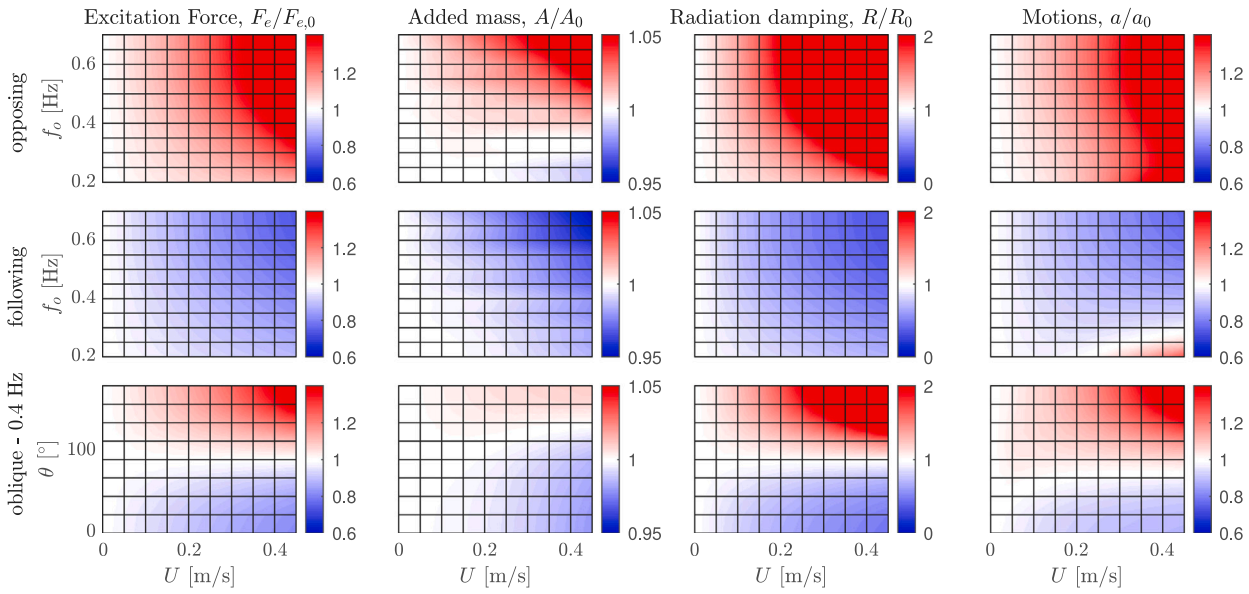

Fig. 16. Horizontal component of hydrodynamic coefficients and motions as a function of wave–current condition. Shown for conditions equivalent to experiments and normalised by the values in zero current for the presented value of frequency/direction.

of the VIM reported along with the dependency on the mooring line stiffness and configuration, further work is required to conclude on the effect of VIM on full-scale wave buoy measurement.

Wave-induced motion amplitudes were extracted from FFTs to assess the wave–current–buoy interaction along with the performance of three methods aimed at predicting the wave-induced buoy response in current. Mooring resonance effects are identified for low wave frequencies which cause deviation from linear wave–current theory motion predictions, but is captured using a frequency-domain hydrodynamic coefficient (HC) based model. In general all three methods agree well with experimental data other than for opposing wave–current conditions. For these higher wavenumber and steepness conditions, counter-intuitively large horizontal motions are observed which are also predicted using the HC model. These large motions are concluded to be a result of larger particle accelerations and excitation forces owing to the high wavenumbers. A large heave response is also observed for the high-frequency opposing wave–current conditions, which is likely a result of nonlinear forcing in higher steepness conditions which is not captured using any of the approaches tested.

These experiments and the subsequent analysis highlights the mechanism and potential for VIM to alter the apparent wave field, and demonstrates altered dynamics in the presence of current which will introduce significant errors if not accounted for in post-processing (in addition to errors highlighted from the lack of knowledge of the current and current-modified wavenumbers). Subsequently, this paper quantifies the performance of two methods which may be implemented in post-processing approaches (e.g. Pillai et al. (2021)) to account for the effect of current and predict the velocity. If successfully implemented, this has the potential to significantly reduce the errors in wave parameters estimated from wave buoy measurements and increase our understanding of the wave–current environment.

Declaration of interests

The authors declare that they have no known competing financial interests or personal relationships that could have appeared to influence the work reported in this paper.

CRediT authorship contribution statement

S. Draycott: Conceptualization, Methodology, Software, Validation, Formal analysis, Investigation, Writing – original draft, Visualization, Funding acquisition. **A.C. Pillai:** Conceptualization, Investigation, Writing – review & editing, Funding acquisition. **R. Gabl:** Formal analysis, Methodology, Writing – review & editing. **P.K. Stansby:** Methodology, Writing – review & editing. **T. Davey:** Conceptualization, Investigation, Methodology, Writing – review & editing, Funding acquisition.

Acknowledgements

This work is funded in part by the EPSRC Supergen Offshore Renewable Energy Hub [grant no: EP/S000747/1] Flexible Fund support for *Accounting for Current in Wave Buoy Measurements*. S. Draycott acknowledges a Dame Kathleen Ollerenshaw Fellowship. The authors would like to thank Dr Laura-Beth Jordan and Martyn Lennon at the FloWave Ocean Energy Research Facility for their help in preparing and executing the experiments.

References

Al-Solihat, M.K., Nahon, M., 2016. Stiffness of slack and taut moorings. Ships Offshore Struct. 11 (8), 890–904.

Babarit, A., Delhommeau, G., 2015. Theoretical and numerical aspects of the open source BEM solver NEMOH. In: 11th European Wave and Tidal Energy Conference. EWTEC2015.

Behara, S., Sotiropoulos, F., 2016. Vortex-induced vibrations of an elastically mounted sphere: the effects of Reynolds number and reduced velocity. J. Fluids Struct. 66, 54–68.

Benoit, M., Frigaard, P., Schaffer, H.A., 1997. Analyzing multidirectional wave spectra: a tentative classification of available methods. In: Proceedings of the 1997 IAHR Conference. pp. 131–158.

Bernitsas, M.M., Garza-Rios, L.O., 1996. Effect of mooring line arrangement on the dynamics of spread mooring systems. J. Offshore Mech. Arct. Eng. 118 (1), 7–20. http://dx.doi.org/10.1115/1.2828806.

Bruserud, K., Haver, S., Myrhaug, D., 2018. Joint description of waves and currents applied in a simplified load case. Mar. Struct. 58, 416–433.

Bunney, C., 2011. A High Resolution SWAN Model Assessment: north Norfolk to Humber. Met Office Forecasting Research Technical Report, 557.

Chen, H., Zou, Q., 2019. Effects of following and opposing vertical current shear on nonlinear wave interactions. Appl. Ocean Res. 89, 23–35.

Draycott, S., Noble, D., Davey, T., Bruce, T., Ingram, D., Johanning, L., Smith, H., Day, A., Kaklis, P., 2018a. Re-creation of site-specific multi-directional waves with non-collinear current. Ocean Eng. 152, 391–403.

Draycott, S., Payne, G., Steynor, J., Nambiar, A., Sellar, B., Venugopal, V., 2019. An experimental investigation into non-linear wave loading on horizontal axis tidal turbines. J. Fluids Struct. 84, 199–217.

Draycott, S., Steynor, J., Davey, T., Ingram, D.M., 2018b. Isolating incident and reflected wave spectra in the presence of current. Coast. Eng. J. 60 (1), 39–50.

Draycott, S., Steynor, J., Nambiar, A., Sellar, B., Venugopal, V., 2020. Rotational sampling of waves by tidal turbine blades. Renew. Energy 162, 2197–2209.

Draycott, S., Sutherland, D., Steynor, J., Sellar, B., Venugopal, V., 2017. Re-creating waves in large currents for tidal energy applications. Energies 10 (11), 1838.

Gonçalves, R.T., Rosetti, G.F., Fujarra, A.L., Oliveira, A.C., 2013. Experimental study on vortex-induced motions of a semi-submersible platform with four square columns, part II: Effects of surface waves, external damping and draft condition. Ocean Eng. 62, 10–24.

Gonzales, F.I., 1984. A case study of wave-current-bathymetry interactions at columbia river entrance. J. Phys. Oceanogr. 14, 1065–1078.

Gottlieb, O., Yim, S.C., 1992. Nonlinear oscillations, bifurcations and chaos in a multi-point mooring system with a geometric nonlinearity. Appl. Ocean Res. 14 (4), 241–257.

Govardhan, R., Williamson, C., 2005. Vortex-induced vibrations of a sphere. J. Fluid Mech. 531, 11.

Hong, Y., Choi, Y., Lee, J., Kim, Y., 2008. Vortex-induced motion of a deep-draft semi-submersible in current and waves. In: The Eighteenth International Offshore and Polar Engineering Conference. OnePetro.

Jonsson, I., Brink-Kjaer, O., Thomas, G., 1978. Wave action and set-down for waves on a shear current. J. Fluid Mech. 87 (3), 401–416.

Jonsson, I.G., Skougaard, C., Wang, J.D., 1970. Interaction between waves and currents. Coast. Eng. 1970 489–507. http://dx.doi.org/10.2307/j.ctvfrxqp9.34.

Kirby, J.T., Chen, T.-M., 1989. Surface waves on vertically sheared flows: approximate dispersion relations. J. Geophys. Res. Oceans 94 (C1), 1013–1027.

Koop, A., de Wilde, J., Fujarra, A.L.C., Rijken, O., Linder, S., Lennblad, J., Haug, N., Phadke, A., 2016. Investigation on reasons for possible difference between VIM response in the field and in model tests. In: International Conference on Offshore Mechanics and Arctic Engineering, Vol. 49934. American Society of Mechanical Engineers, V002T08A059.

Lee, H., Thompson, M.C., Hourigan, K., 2008. Vortex-induced vibrations of a tethered sphere with neutral buoyancy. In: Proceedings of the XXIIth International Congress on Theoretical and Applied Mechanics. ICTAM 2008, Adelaide, Australia, p. 11299.

Lewis, M.J., Palmer, T., Hashemi, R., Robins, P., Saulter, A., Brown, J., Lewis, H., Neill, S., 2019. Wave-tide interaction modulates nearshore wave height. Ocean Dyn. 69 (3), 367–384.

Li, Y., Ellingsen, S.A., 2019. A framework for modeling linear surface waves on shear currents in slowly varying waters. J. Geophys. Res. Oceans 124 (4), 2527–2545.

Macisaac, C., Naeth, S., 2013. TRIAXYS Next wave II directional wave sensor the evolution of wave measurements. In: 2013 OCEANS - San Diego. MTS, pp. 1–8. http://dx.doi.org/10.23919/OCEANS.2013.6741003.

Martin, B., Rijken, O., 2012. Experimental analysis of surface geometry, external damping and waves on semisubmersible vortex induced motions. In: International Conference on Offshore Mechanics and Arctic Engineering, Vol. 44922. American Society of Mechanical Engineers, pp. 809–816.

Masson, D., 1996. A case study of wave–current interaction in a strong tidal current. J. Phys. Oceanogr. 26 (3), 359–372.

Noble, D.R., Davey, T., Smith, H.C., Kaklis, P., Robinson, A., Bruce, T., 2015. Spatial variation in currents generated in the FloWave ocean energy research facility. In: Proceedings of the 11th European Wave and Tidal Energy Conference. EWTEC2015, Nantes, France, pp. 6–11.

Olabarrieta, M., Medina, R., Castanedo, S., 2010. Effects of wave–current interaction on the current profile. Coast. Eng. 57 (7), 643–655.

Peregrine, D.H., 1976. Interaction of water waves and currents. Adv. Appl. Mech. 16, 9–117.

Pillai, A.C., Davey, T., Draycott, S., 2021. A framework for processing wave buoy measurements in the presence of current. Appl. Ocean Res. 106, 102420.

Raghavan, K., Bernitsas, M., 2011. Experimental investigation of Reynolds number effect on vortex induced vibration of rigid circular cylinder on elastic supports. Ocean Eng. 38 (5–6), 719–731.

Rajamuni, M.M., Thompson, M.C., Hourigan, K., 2020. Vortex dynamics and vibration modes of a tethered sphere. J. Fluid Mech. 885.

Sareen, A., Zhao, J., Jacono, D.L., Sheridan, J., Hourigan, K., Thompson, M.C., 2018a. Vortex-induced vibration of a rotating sphere. J. Fluid Mech. 837, 258–292.

Sareen, A., Zhao, J., Sheridan, J., Hourigan, K., Thompson, M., 2018b. Vortex-induced vibrations of a sphere close to a free surface. J. Fluid Mech. 846, 1023–1058.

Smith, J.M., 1997. One-Dimensional Wave-Current Interaction. Technical Report, Engineer Research and Development Center Vicksburg Ms Coastal and Hydraulics Lab.

Song, H., Kuang, C., Wang, X.H., Ma, Z., 2020. Wave-current interactions during extreme weather conditions in southwest of bohai bay, China. Ocean Eng. 216, 108068.

Sutherland, D.R., Noble, D.R., Steynor, J., Davey, T., Bruce, T., 2017. Characterisation of current and turbulence in the FloWave ocean energy research facility. Ocean Eng. 139, 103–115.

Toffoli, A., Waseda, T., Houtani, H., Kinoshita, T., Collins, K., Proment, D., Onorato, M., 2013. Excitation of rogue waves in a variable medium: An experimental study on the interaction of water waves and currents. Phys. Rev. E 87 (5), 051201.

Tolman, H.L., 1990. Effects of tides and storm surges on north sea wind waves. J. Phys. Oceanogr. 21, 766–781.

Tucker, M.J., Pitt, E.G., 2001. Waves in Ocean Engineering, Vol. 5.

Umar, A., Datta, T., 2003. Nonlinear response of a moored buoy. Ocean Eng. 30 (13), 1625–1646.

Veras Guimarães, P., Ardhuin, F., Sutherland, P., Accensi, M., Hamon, M., Pérignon, Y., Thomson, J., Benetazzo, A., Ferrant, P., 2018. A surface kinematics buoy (SKIB) for wave–current interaction studies. Ocean Sci. 14 (6), 1449–1460.

Wang, D.W., Liu, A.K., Chih, Y.P., Meindl, E.A., 1994. Wave-current interaction near the gulf stream during the surface wave dynamics experiment. J. Geophys. Res. 99 (C3), 5065–5079. http://dx.doi.org/10.1029/93JC02714.

White, B.S., Fornberg, B., 1998. On the chance of freak waves at sea. J. Fluid Mech. 355, 113–138.

Yim, S.C., Yuk, D., Naess, A., Shih, I., et al., 2008. Stochastic analysis of nonlinear responses of a moored structure under narrow band excitations. J. Offshore Mech. Arct. Eng. 130 (1).